Room-temperature ballistic transport in III-Nitride heterostructures

Elison Matioli[1,*] and Tomás Palacios[1,†]

[1] *Department of Electrical Engineering and Computer Science, Massachusetts Institute of Technology, Cambridge, 02139 MA, USA*

Room-temperature (RT) ballistic transport of electrons is experimentally observed and theoretically investigated in III-Nitrides. This has been largely investigated at low temperatures in low band-gap III-V materials due to their high electron mobilities. However their application to RT ballistic devices is limited by the low optical phonon energies, close to KT at 300 K. In addition, the short electron mean-free-path at RT requires nanoscale devices for which surface effects are a limitation in these materials. We explore the unique properties of wide-band-gap III-Nitride semiconductors to demonstrate RT ballistic devices. A theoretical model is proposed to corroborate experimentally their optical phonon energy of 92 meV, which is $\sim$ 4x-larger than in other III-V semiconductors. This allows RT ballistic devices operating at larger voltages and currents. An additional model is described to determine experimentally a characteristic dimension for ballistic transport of 188 nm. Another remarkable property is their short carrier depletion at device sidewalls, down to 13 nm, which allows top-down nanofabrication of very narrow ballistic devices. These results open a wealth of new systems and basic transport studies possible at RT.

Ballistic transport has attracted huge interest of the research community since electrons can propagate through the semiconductor without random scattering from lattice defects, impurities and phonons. This regime was referred to as electron optics[1] and occurs when electrons travel a distance shorter than their mean free path L_m, defined as the average distance travelled between consecutive scatterers.

Semiconductors presenting very high electron mobility have been used as means to investigate ballistic and other transport phenomena. Most of these studies were undertaken at low temperatures where L_m can be quite large, on the order of a few microns[2]. Moreover, low temperature operation was required due to the very low optical phonon energies, close to KT at 300 K, of semiconductors such as Arsenides and Antimonides. In addition, the conductance is quantized at low temperatures, fundamentally similar to the quantized Hall effect[3], where only a small number of transverse quantum channels are occupied. These effects have been explored and demonstrated in a number of different devices based on quantum interference[4, 5], quantized conductance in a point contact[6, 7], electron focusing[8], negative bend resistance[9, 10], quenched and negative Hall effects[11], and lateral hot ballistic electron[12].

While these devices were demonstrated under low temperature, ballistic transport at RT would open a pathway for many practical applications[13–16], offering a new design space for high frequency devices with quicker switching responses and lower dissipation losses than conventional devices. At RT however, L_m is largely reduced, below 100 nm in some III-V semiconductors. This requires much smaller device dimensions, where surface effects can be a limiting factor[17]. The large depletion of carriers near etched sidewalls of the device, typically over 100 nm due to

* elison.matioli@polytechnique.org
† tpalacios@mit.edu

the relatively small carrier concentrations, poses severe limitations for top-down fabrication in several materials such as GaAs-AlGaAs and InSb-AlInSb[18, 19]

Another important consideration for RT ballistic devices is the energy at which optical phonons are emitted by electrons. Ballistic transport is largely degraded above such energy, when electrons are strongly scattered by the crystal lattice through the emission of optical phonons. This limits the use of many materials as ballistic devices operating at RT due to their low optical phonon energy, close to KT, such as 25 meV in InSb/AlInSb[19], 33 meV in InGaAs/InP[20], 27 meV in InAs [17] and 19 meV in Si/SiGe[21].

In this work, we demonstrate for the first time that the high electron mobility in wide band-gap materials, such as in III-Nitrides, coupled to their very high optical phonon energies ($\sim$ 4x-larger than in other III-V semiconductors) allows the observation of ballistic transport at RT. Ballistic devices have been largely investigated in low-band gap III-V materials where their reduced effective mass results in higher mobilities. Here, we show that the high optical phonon energy of wide band-gap III-Nitrides ($\hbar w_{\rm op} = 92$ meV) allows ballistic transport of electrons with much larger energy even at RT. A pronounced ballistic transport at RT was demonstrated in III-Nitride heterostructures using top-down nanofabrication, which is enabled due to the very short depletion of carriers at etched sidewalls. This is a remarkable property of III-Nitrides allowing electronic conduction in top-down nanoscale devices, not found in semiconductors such as Arsenides or Antimonides, where the depletion of carriers at etched sidewalls extends over hundreds of nanometers. Using state-of-the-art nanofabrication technology, we demonstrate high-quality nanoscale ballistic filters with dimensions down to 33 nm, much shorter than the mean free path of electrons at RT. In combination to experimental results, theoretical models were proposed to determine the optical phonon energy from the current density and the characteristic ballistic length from the bend resistance in these devices. The former offers a robust method to assess experimentally the optical phonon energy independently on the device geometry and clears some misconceptions found in previous works. The latter offers a more direct quantification of the dimensions for ballistic transport than the theoretical L_m. This first demonstration of high-energy electrons under ballistic transport at RT combined to the unique suitability of III-Nitrides for top-down nanofabrication opens new opportunities for advanced semiconductor devices presenting higher frequencies and lower power dissipation operating at RT.

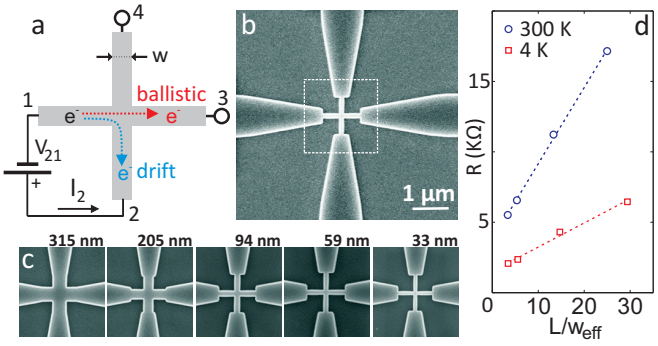

FIG. 1. a. Schematic of the device operation under drift and ballistic transports. Electrons under drift transport flow toward lead 2 and under ballistic transport flow forward, toward lead 3. b. SEM images of 1 μm-long nanoscale crosses. c. Close-up SEM images of nanoscale crosses with widths w varying from 315 nm to 33 nm. (d) Two-terminal resistance R versus $L/w_{\rm eff}$ for both 300 K and 4 K. Dashed lines correspond to the model $R = R_c + R_{\rm sh}L/w_{\rm eff}$ from where the parasitic resistance R_c and the depletion width at cross sidewalls $w_{\rm dep}$ were extracted.

The electronic transport was investigated by fabricating nanoscale crosses with dimensions close to L_m (Figure 1) combined with temperature-dependent measurements. The principle of operation of the device is the following:

Under diffusive regime, electrons flow from leads 1 to 2, following the electric field created in the cross by the applied voltage V_{21} (blue dotted arrow in Figure 1a). This induces a potential V_{34}, between leads 3 and 4, of the same sign as the applied V_{21}. This is equivalent to the voltage drop at a small resistance $R_{\rm cross}$ present at the center of the cross, which can be written as $\mathrm{V}_{34}^{\rm drift}$=$R_{\rm cross}\, I_2$.

When the cross width w is reduced below L_m, a large number of electrons is injected ballistically into the opposite lead 3 (red dotted arrow in Figure 1a) since there are much fewer scattering events to change their momentum along the electric field. This induces a negative potential in lead 3 relative to lead 4, thus a V_{34} of opposite sign relative to V_{21}. This is equivalent to a negative bend resistance R_b at the center of the cross[22] - a signature of ballistic transport - creating a negative potential $\mathrm{V}_{34}^{\rm ballistic}$=$R_b\, I_2$. Thus, this cross geometry offers a way to decouple ballistic from drift transport, operating as a filter for ballistic electrons.

The devices investigated in this work were fabricated on $In_{0.17}Al_{0.83}N$/GaN on SiC substrate. The epitaxial structure was composed of InAlN (7.3 nm)/ AlN (1 nm)/ GaN (10 nm)/ InGaN (3.3 nm)/ GaN (1.8 μm), where the InGaN layer acts as a back-barrier to improve confinement of electrons in the two-dimensional electron gas (2DEG)[23]. Nanoscale crosses with length of 1 μm and widths of 315 nm, 205 nm, 94 nm, 59 nm and 33 nm (these were measured dimensions after fabrication) were first defined by electron-beam lithography on hydrogen silsesquioxane 2% (HSQ) (Figures 1b-c). This served as a hard mask for Cl_2-based etch of the surrounding material (200 nm-deep) to isolate different devices. The dimensions of the crosses were chosen based on the estimated L_m, calculated from the Fermi velocity of electrons using the semi-classical expression $L_m = v_F\tau = \sqrt{2\pi n}\hbar\mu/q$. The electron concentration n and mobility μ in the 2DEG were determined from temperature-dependent Hall measurements as n = 1.51x10^{13} (1.24x10^{13}) cm^{-2} and μ = 3476 (1285) cm^2/Vs, and the estimated L_m was 223 nm (75 nm) at 4 K (300 K). A Ti (200 Å)/Al (1000 Å)/Ni (250 Å)/Au (500 Å) metal stack was deposited over large mesa structures (60 μm-wide) connected to the four nanoscale leads and annealed at 845^{o}C to form ohmic contacts.

The contact resistance R_c and sidewall depletion width $w_{\rm dep}$ were determined from the linear dependence of the two-terminal resistance versus the ratio of length L over the effective width $w_{\rm eff} = w - w_{\rm dep}$ using the following model

$$R = R_c + R_{\rm sh}L/(w - w_{\rm dep}) \tag{1}$$

where $R_{\rm sh}$ is the equivalent sheet resistance in the cross and $w_{\rm dep}$ is the depletion width formed at both etched sidewalls which effectively shrinks the nominal cross width w. This model is plotted in dashed lines in Figure 1d, at both 300 K and 4 K, which resulted in R_c of 3747 Ω at 300 K and 1522 Ω at 4 K (R_c is similar for all devices and includes contact and other parasitic resistances). The voltage drop in the nanoscale cross was determined after removing the voltage drop in R_c as $V_{\rm wire} = V_{21} - R_c I_2$. Equation (1) was also used to determine $w_{\rm dep}$, resulting in values between 19 nm and 26 nm obtained from the linear dependence of $1/(R - R_c)$ versus w. The shorter $w_{\rm dep}$ compared to other material systems[18, 19] is due to the larger carrier concentration in the 2DEG in III-Nitride heterostructures which allows the top-down nanofabrication of much narrower devices. In this case, the narrowest cross (33 nm-wide) was depleted of carriers at all temperatures, impeding its electrical characterization.

Ballistic transport was probed in two ways: (1) By lowering the temperature which increases L_m; (2) By reducing the cross width below L_m. The transport was measured by applying voltage independently in two adjacent orthogonal leads 1 and 2, in a push-pull configuration with $V_2 = -V_1$, and by measuring the induced voltage in leads 4 and 3

with $I_3 = I_4 = 0$. The samples were measured in a micro-manipulated cryogenic probe station from Lake Shore, at temperatures varying from 300 K to 4 K cooled with liquid Helium.

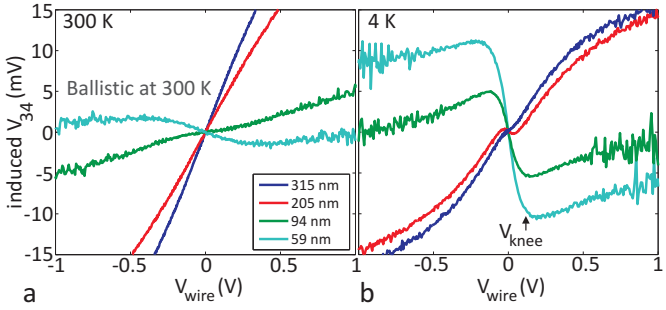

FIG. 2. Induced voltage V_{34} versus applied voltage V_{wire} for 1 μm-long crosses on InAlN/GaN heterostructure. (a) Room temperature measurement showing a change from drift (positive slope) to ballistic transport (negative slope) as the cross width is reduced. (b) Measurement at 4 K indicating much more pronounced ballistic transport.

Figures 2 shows the measurement of V_{34} versus V_{wire}. At RT, the transport was determined by drift in the wide crosses, which is indicated by the linear positive slope of V_{34} with respect to V_{wire} for the 315 nm-, 205 nm- and 94 nm-wide crosses (Figure 2a). A clear transition from drift to ballistic transport is observed in the 59 nm-wide cross, indicated by the negative slope of V_{34}. This is an important observation of ballistic transport at RT for the 59 nm-wide cross (Figure 2a), which is in agreement with L_m of 75 nm at RT. When the temperature was lowered to 4 K, L_m increased from 75 nm to 223 nm, and a pronounced ballistic transport was observed for the 94 nm- and 59 nm-wide crosses by the negative slope of V_{34} versus V_{wire}, corresponding to a negative bend resistance (Figure 2b). Despite its smaller dimension than L_m, the 205 nm-wide cross only showed a very mild negative slope of V_{34}. More representative than L_m is the characteristic ballistic length L_b which is defined and experimentally determined later in this paper.

The negative bend resistance is observed for $V_{\text{wire}} < V_{\text{knee}}$ (Figure 2b), after which electrons have enough energy to emit optical phonons which changes both their energy and momentum (schematic in Figure 2c), reducing the effective mean free path of electrons due to electron-phonon scattering and undermining their ballistic transport. The energy qV_{knee} is often attributed in the literature directly to the energy of optical phonons[20, 21] as $\hbar w_{\text{op}} \approx qV_{\text{knee}}$.

However, in the present case, the observed $V_{\text{knee}} \sim 126$ mV was much larger than the expected 92 mV of III-Nitrides. In addition, similar measurements performed in longer crosses with 5 μm fabricated in the same material resulted in a much less pronounced ballistic effect as well as in a much larger V_{knee}, close to 500 mV (see Supplementary Information). These results show that V_{knee} extracted from such measurements cannot be directly assigned to $\hbar w_{\text{op}}$, since the energy of electrons crossing the center portion of the crosses, where the transport is probed, is smaller than the energy qV_{knee} applied at the leads (electrons scatter and lose part of their energy during their propagation to the center of the crosses).

The current density $J_2 = I_2/w$ is a more consistent variable to look at these effects since it is not dependent on the cross geometry. Unlike V_{knee}, the current density J_2^* corresponding to the transition between diffusive and ballistic regimes in the plot of V_{34} versus J_2 (Figure 3), was similar for 1 μm- and 5 μm-long crosses (see Supplementary Information), which motivated us to propose an alternative method to extract $\hbar w_{\text{op}}$ directly from J_2. J_2 in a 2DEG can be written as the product of the density of states, group velocity $\hbar k/m^*$ (where m^* is the effective mass of

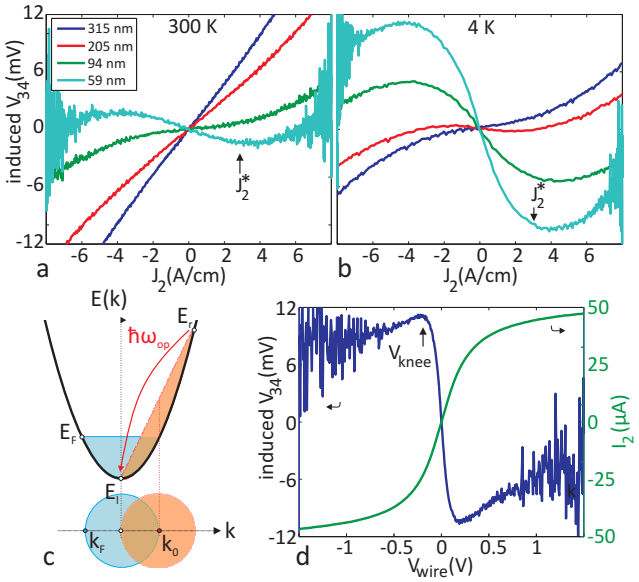

FIG. 3. Induced voltage versus current density. a. V_{34} versus J_2, normalized by cross width for 1μm-long crosses on InAlN/GaN heterostructure at 300 K. b. Similar measurements at 4 K. c. Schematic of the band structure representing the optical phonon emission by high-energy electrons. d. V_{34} and I_2 versus V_{wire} for 59 nm-wide cross on InAlN/GaN showing current saturation when optical phonons are emitted.

electrons in GaN) and occupation probability function $f_k(k)$ integrated over all states in k-space as

$$J_2 = \frac{2q}{4\pi^2}\int_k \frac{\hbar k}{m^*} f(k)dk = qn_s\frac{\hbar k_0}{m^*} \tag{2}$$

where k_0 corresponds to the geometrical centroid of the occupied area in k-space[24]. In this approach, the geometrical centroid k_0 incorporates the averaged effect of non-uniformities of the potential distribution in the nanocrosses[25], present especially at their corners.

At large enough applied bias, ultra-fast optical phonon emission in GaN fixes the difference of quasi-Fermi levels[24] as E_r-E_l=$\hbar\omega_{\rm op}$, where an electron at the right-going state E_r is scattered to the lowest available left-going state E_l in the band structure (Figure 3c). At this moment, the current I_2 starts slowly to saturate and the slope of V_{34} changes sharply at $V_{\rm knee}$, as observed in Figure 3d. The optical phonon energy can be written as the difference in electron energy at E_r and E_l as:

$$\hbar\omega_{\rm op} = E_r - E_l = \frac{\hbar^2(k_F + k_0^*)^2}{2m^*} - \frac{\hbar^2(k_F - k_0^*)^2}{2m^*} \tag{3}$$

where k_F is the Fermi wavevector given by $k_F = \sqrt{2\pi n}$ and n is the carrier density in the 2DEG. The geometrical centroid k_0^*, at which optical phonon emission starts happening, can be determined from the current density J_2^*, at which current starts saturating, using Equation (2):

$$k_0^* = J_2^* m^*/\hbar q n_s \tag{4}$$

Thus, $\hbar\omega_{\mathrm{op}}$ can be calculated from J_2^* using Equations (3) and (4). In the measurement from Figure 3b, $J_2^* = 2.86$ A/cm, which corresponds precisely to the current density where $V_{\mathrm{knee}} = 126$ mV. This results in $\hbar\omega_{\mathrm{op}}$ of 95.1 meV which is very close to the optical phonon energy of III-Nitrides.

The induced voltage was also modelled as a function of the current density as $V_{34} = \mathrm{V}_{34}^{\mathrm{drift}} + \mathrm{V}_{34}^{\mathrm{ballistic}}$. The drift component was written as $V_{34}^{\mathrm{drift}} = \rho_{\mathrm{cross}} J_2$, where $\rho_{\mathrm{cross}} = R_{\mathrm{cross}} w$, and the ballistic component $\mathrm{V}_{34}^{\mathrm{ballistic}} = w R_b J_2$, thus:

$$V_{34} = w(R_{\mathrm{cross}} + R_b)\, J_2 \tag{5}$$

A great deal of information can be obtained by modelling the bend resistance R_b, which is proportional to the transmission probability of a ballistic electron to the opposite lead[18]. An expression for R_b can be written using Büttiker-Landauer's approach[26] as $R_b = R_t(T_S - T_F)/\left[4T_S(T_S + T_F)\right]$, where $R_t = \pi h/(2e^2 k_F w)$ is the two-terminal resistance of a quantum wire of width w. T_F and T_S are the transmission probability of electrons going forward and sideways respectively. These probabilities are very sensitive to the amount of scattering at the center of the cross. Under diffusive transport, electrons are scattered randomly in all direction, hence $T_S = T_F \approx 1/4$, thus $R_b \approx 0$ and $V_{34} = \mathrm{V}_{34}^{\mathrm{drift}}$. Under ballistic transport, the forward-going transmission probability is increased by the ballistic probability as $T_F = 1/4 + T_b$. The bend resistance can then be simplified[27] as $R_b = -2R_t T_b$, which is negative as first predicted by M. Büttiker[22]. The term T_b can be written as[18, 28, 29] $T_b = \int_{-\theta_c}^{\theta_c} f_\theta(\theta) d\theta \exp(-w/L_b)$ where here a ballistic length L_b is introduced, which represents a characteristic dimension under which electron transport is ballistic (similarly to the mean free path). The angular distribution of electrons injected forward is given by the function $f_\theta(\theta)$ which can be approximated[15] by $\cos(\theta)/2$, where $\theta_c = \mathrm{atan}(1/2)$ corresponds to the range of angles for which electrons can be transmitted to the forward lead (inset of Figure 4). After integration, $T_b = 0.45\, \exp(-w/L_b)$. Thus,

$$R_b = -0.9\, \exp(-w/L_b) \frac{h}{2e^2} \frac{\pi}{k_F w_{\mathrm{eff}}} \tag{6}$$

where the effective width $w_{\mathrm{eff}} = w - w_{\mathrm{dep}}$ accounts for the sidewall depletion.

At 300 K, for crosses much larger than L_b, $R_b \approx 0$ thus, from Equation (5), V_{34} has a positive slope equal to ρ_{cross}. For the 315 nm-wide cross at 300 K, $\rho_{\mathrm{cross}} = 2.4$ mΩcm ($R_{\mathrm{cross}} = 76.2$ Ω) (Figure 3a). When the cross width is reduced below L_b, still at 300 K, the fraction of ballistic electrons increases as $\exp(-w/L_b)$ but V_{34}^{drift} remains the same since the normalized ρ_{cross} is nearly constant, leading to a negative slope of V_{34} versus J_2 (Figure 3a). On the other hand, when the temperature is lowered, both ballistic and drift terms change. The mobility of electrons increases, which reduces ρ_{cross}. In addition, L_b increases which increases the fraction of ballistic electrons going to the lead 3, thus $|R_b| \gg R_{\mathrm{cross}}$ yielding a much more apparent ballistic effect at low temperatures (Figure 3b) and $V_{34} \sim \mathrm{V}_{34}^{\mathrm{ballistic}}$ (Equation (5)).

Equation (6) offers a direct way to determine experimentally the characteristic ballistic length L_b which was extracted from the slope of the experimental $w_{\mathrm{eff}}|R_b|$ versus w in logarithmic scale (Figure 4a), resulting in L_b of 143 nm for InAlN/GaN at 4 K. This model is only valid for $|R_b| \gg R_{\mathrm{cross}}$, thus not applicable for the 315 nm-wide crosses.

To check their consistency, these models were applied to another III-Nitride heterostructure, consisting of

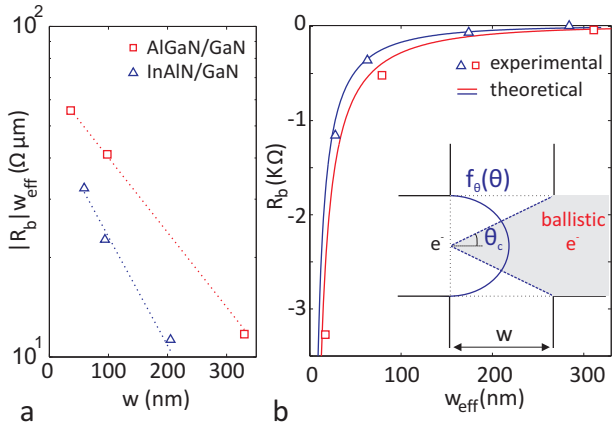

FIG. 4. Experimental determination of the characteristic ballistic length for both heterostructures. a. Logarithmic scale plot of $w_{\rm eff}|R_b|$ versus w for both InAlN/GaN and AlGaN/GaN heterostructures at 4 K. The characteristic ballistic length L_b was extracted from the slope of these curves. b. Bend resistance R_b versus effective cross width $w_{\rm eff} = w - w_{\rm dep}$ (squares for AlGaN/GaN and triangles for InAlN/GaN), along with the theoretical curves (solid lines). (Inset) Schematic of the ballistic transmission of electrons to the opposite lead in these crosses.

$Al_{0.25}Ga_{0.75}N$ (25 nm)/ AlN (8 nm) /GaN on Silicon substrate which presented larger μ and L_m. The 2DEG formed at the heterostructure interface presented n = 1.10x10^{13} cm^{-2}, μ = 5151 cm^2/Vs at 4 K and an estimated L_m of 281 nm. A similar transition from drift to ballistic transport was observed, where for completeness, the full temperature-dependent measurement at 300 K, 150 K, 77 K, 50 K and 4 K is shown in the Supplementary Information. For this structure, J_2^* = 2.40 A/cm (see Supplementary Information), resulting in $\hbar\omega_{op}$ = 93 meV, which is again in agreement with $\hbar w_{\rm op}$ of III-Nitrides despite the different heterostructure, electron mobility and carrier density. L_b extracted from the slope of $w_{\rm eff}|R_b|$ versus w was equal to 188 nm for AlGaN/GaN (Figure 4a). The larger L_b in AlGaN/GaN compared to InAlN/GaN is due to its higher electron mobility, thus larger L_m. In both cases, the measured L_b was shorter than the estimated L_m which is likely due to extra scattering mechanisms that reduce the electron mobility[25], such as at etched sidewalls, and are not taken into account in the model based on the Fermi velocity. Hence, L_b can be used to measure experimentally the effect of scattering mechanisms that cannot be estimated with L_m.

The theoretical R_b from Equation (6) was plotted after determining L_b and agreed well with the experimental values of bend resistance for both materials, as shown in Figure 4b. This model corroborates the ballistic nature of the transport measured in these structures and offers an analytical expression of R_b which can be used in the design of future ballistic devices.

In conclusion, high-quality nanoscale ballistic filters, with dimensions down to 33 nm, were used to demonstrate for the first time ballistic electronic devices operating at room temperature (RT) in III-Nitride semiconductors. These nanoscale devices presenting dimensions much shorter than the mean free path of electrons at RT were fabricated using state-of-the-art top-down nanofabrication technology, which was possible due to the very short depletion of carriers at etched sidewalls. This is a remarkable property of III-Nitrides allowing electronic conduction in very narrow devices, which is not found in other semiconductors such as Arsenides or Antimonides. More importantly, this work highlights that high electron mobility in wide band-gap materials, such as in III-Nitrides, coupled to their very high optical phonon energies - $\sim$ 4x-larger than in other III-V semiconductors - allows ballistic transport at RT of electrons with higher energy than in other III-V semiconductors.

Complementing our experimental results, we proposed a theoretical model to determine the optical phonon energy from the current density across the device, which was applied to both InAlN/GaN and AlGaN/GaN heterostructures. The results were in very good agreement with the $\hbar w_{\rm op} = 92$ meV in III-Nitrides, revealing a much more consistent method than assigning the optical phonon energy directly to $qV_{\rm knee}$, as often found in the literature. In addition, a model of the bend resistance was described and used to determine the characteristic ballistic length L_b. This method offered an experimental quantification of the dimensions for ballistic transport. The measured L_b of 143 nm for InAlN/GaN and 188 nm for AlGaN/GaN heterostructures were shorter than the estimated L_m revealing the presence of extra scattering mechanisms, such as at etched sidewalls, that were not taken into account in the semi-classical model based on the Fermi velocity.

This work opens a wealth of new systems and basic transport studies possible at RT in wide band-gap semiconductors, and offers new opportunities for advanced semiconductor devices operating at higher frequencies and lower power dissipation operating at RT.

I. AUTHOR INFORMATION

Corresponding Author:

email: elison.matioli@polytechnique.org

II. ACKNOWLEDGEMENT

We thank Omair Saadat and James Teherani from the Massachusetts Institute of Technology, Debdeep Jena from the University of Notre Dame, Claude Weisbuch from the University of California Santa Barbara, Hongwei Li and Dong Lee from Veeco Instruments, and Xiang Gao and Shiping Guo from IQE RF LLC for fruitful discussions and assistance with experiments. The authors acknowledge partial support from the DARPA NEXT and ONR YIP programs.

[1] H. van Houten and C. W. J. Beenakker, *Analogies in Optics and Microelectronics*, Kluwer Academic, Dordrecht, (1990).

[2] C. W. J. Beenakker and H. van Houten. *Solid State Physics*, 44, 1, (1991).

[3] H. L. Stormer and D. C. Tsui. *Science*, 220, 1241, (1983).

[4] T. J. Thornton, M. Pepper, H. Ahmed, D. Andrews, and G. J. Davies. *Phys. Rev. Lett.*, 56, 1198, (1986).

[5] Y. Takagaki, K. Gamo, S. Namba, S. Takaoka, K. Murase, and S. Ishida. *Solid State Commun.*, 71, 809, (1989).

[6] B. J. van Wees, H. van Houten, C. W. J. Beenakker, J. G. Williamson, L. P. Kouwenhoven, D. van der Marel, and C. T. Foxon. *Phys. Rev. Lett.*, 60, 848, (1988).

[7] R. de Picciotto, H. L. Stormer, L. N. Pfeiffer, K. W. Baldwin, and K. W. West. *Nature*, 411, 3, (2001).

[8] H. van Houten, C. W. J. Beenakker, P. H. M. van Loosdrecht, T. J. Thornton, H. Ahmed, M. Pepper, C. T. Foxon, and J. J. Harris. *Phys. Rev. B*, 37, 8534, (1988).

[9] G. Timp, H. U. Baranger, P. deVegvar, J. E. Cunningham, R. E. Howard, R. Behringer, and P. M. Mankiewich. *Phys. Rev. Lett.*, 60, 2081, (1988).

[10] S. Sasaki, Y. Hirayama, and S. Tarucha. *Jpn. J. Appl. Phys.*, 34, 1351 (1995).

[11] C. J. B. Ford, S. Washburn, M. Büttiker, C. M. Knoedler, and J. M. Hong. *Phys. Rev. Lett.*, 62, 2724, (1989).

[12] A. Palevski, C. P. Umbach, and M. Heiblum. *Appl. Phys. Lett.*, 55, 1421, (1989).

[13] Y. Hirayama and S. Tarucha. *Appl. Phys. Lett.*, 63, 2366, (1993).

[14] A. M. Song, P. Omling, L. Samuelson, W. Seifert, I. Shorubalko, and H. Zirath. *Jpn. J. Appl. Phys.*, 40, L909 (2001).

[15] A. M. Song. *Encyclopedia of Nanoscience and Nanotechnology*, 9,371, (2004).

[16] Q. Diduck, H. Irie, and M. Margala. *International Journal of High Speed Electronics and Systems (IJHSES)*, 19, 23 (2009).

[17] S. Chuang, Q. Gao, R. Kapadia, A. C. Ford, J. Guo, and A. Javey *Nano Lett.*, 13, 555-558 (2013)

[18] Y. Takagaki, S. Tarucha, J. Herfort, and K. Ploog. *Chaos, Solitons and Fractals*, 8, 1359, (1997).

[19] A. M. Gilbertson, A. Kormanyos, P. D. Buckle, M. Fearn, T. Ashley, C. J. Lambert, S. A. Solin, and L. F. Cohen. *Appl. Phys. Lett.*, 99, 242101, (2011).

[20] K. Hieke, J.-O. Wesstrom, E. Forsberg, and C.-F. Carlstrom. *Semiconductor Science and Technology*, 15, 272, (2000).

[21] U. Wieser, S. A. Poenariu, U. Kunze, and T. Hackbarth. *Appl. Phys. Lett.*, 87, 252114, (2005).

[22] M. Buttiker. *IBM Journal of Research and Developments*, 32, 317, (1988).

[23] T. Palacios, A. Chakraborty, S. Heikman, S. Keller, S. P. DenBaars, and U. K. Mishra, *IEEE Elect. Dev. Lett.* , 27, 1, (2006).

[24] T. Fang, R. Wang, H. Xing, S. Rajan, and D. Jena. *IEEE Elect. Dev. Lett.* , 33, 709, (2012).

[25] A. V. Thathachary, N. Agrawal, L. Liu, and S. Datta *Nano Letters* 14, 626 (2014)

[26] M. Buttiker, Y. Imry, R. Landauer, and S. Pinhas. *Phys. Rev. B*, 31, 6207, (1985).

[27] Y. Hirayama, T. Saku, S. Tarucha, and Y. Horikoshi. *Appl. Phys. Lett.*, 58, 2672, (1991).

[28] S. Takaoka, K. Tsukagoshi, S. Wakayama, K. Murase, K. Gamo and S. Namba. *Solid State Commun.*, 83, 775, (1992).

[29] J. Spector, H. L. Stormer, K. W. Baldwin, L. N. Pfeiffer and K. W. West *Surf. Sci.*, 228, 283, (1990)